# **PAPER**

# Multi-objective optimization of a multi-field actuated, multilayered, segmented flexible composite beam

To cite this article: Anil Erol et al 2020 Smart Mater. Struct. 29 024001

View the article online for updates and enhancements.

# You may also like

- Modelling electro-active polymers with a dispersion-type anisotropy
   Mokarram Hossain and Paul Steinmann
- A magneto-active soft gripper with adaptive and controllable motion Xianghao Li, Zheng Zhang, Min Sun et al.
- Actuator placement optimization in an active lattice structure using generalized pattern search and verification
   Cosima Du Pasquier and Kristina Shea

Smart Mater. Struct. 29 (2020) 024001 (14pp)

https://doi.org/10.1088/1361-665X/ab4607

# Multi-objective optimization of a multi-field actuated, multilayered, segmented flexible composite beam

# Anil Erolo, Paris von Lockette and Mary Frecker

The Pennsylvania State University, University Park, PA, United States of America

E-mail: anil.erol.ctr@us.af.mil

Received 21 February 2019, revised 26 July 2019 Accepted for publication 19 September 2019 Published 19 December 2019



#### **Abstract**

Multi-layered, self-actuated devices have been the focus of recent studies due to their ability to exhibit large displacements and achieve complex shapes. Such devices have been constructed using active materials responsive to varying stimuli including electro-active and magneto-active materials to perform useful functions and achieve a wider variety of target shapes compared to single-field actuated unimorph/bimorph structures. However, fabrication of these devices for experimentation is time-consuming and expensive, which warrants the use of simulations as a means of designing high-performing structures. This work seeks to optimize structures employing materials response to magnetic and electric fields for multiple objective functions selected based on the needs of soft robotics applications such as grippers. A multi-objective optimization problem is constructed, utilizing a model developed for any arbitrary number of segments, layers, and material types, accommodating for large displacements and simultaneously applied fields. Three objective functions are chosen: (1) target shape approximation, based on the errors between the coordinates of the computed and desired shapes, (2) cost based on volume of magnetic material, and (3) work performed on a tip-force. The arbitrary optimization problem is reduced to a specific case study containing eight segments to alleviate the computational cost of an unwieldy number of parameters. The parameters are narrowed to: (1) segment lengths, (2) magnetic material in each magneto-active layer. The structure is pre-set to three material types: electro-active polymer, magneto-active elastomer, and a passive substrate. The case study's optimization problem is performed by a genetic algorithm developed by MATLAB for multiple objective functions. The results of the optimization on the case study are analyzed by studying the feasible designs on the Pareto front of the objective functions. Different trade-offs between objective functions are identified, and various feasible designs are found more suitable than others, based on the needs and priorities of an application.

Keywords: optimization, magneto-active, electro-active, multi-objective, electromagnetism

(Some figures may appear in colour only in the online journal)

# Introduction

#### Self-folding structures

Designs of foldable structures in engineering have drawn inspiration from origami, the Japanese art of folding paper, which offers fold patterns that have been employed for centuries [1–3]. Some examples include deformable wheels [4, 5], locomotive worm devices [6], reconfigurable metamaterials [7],

pneumatic actuators [8], and robotic tentacles with 3D mobility [9]. There is a wide range of actuation mechanisms used in Origami-inspired self-folding devices. For example, shape memory materials are commonly used due to their ability to 'remember' an initial shape after deformation, which can be induced by a change in temperature [10]. Other mechanisms include dynamics (i.e. slide-crank mechanisms) [5], pneumatics [11], and responsive polymers [12].

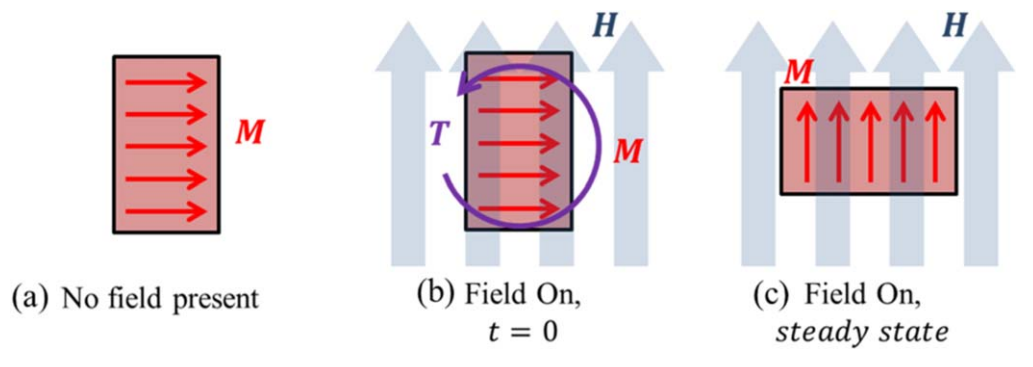


**Figure 1.** A magneto-active body is represented by a rectangle in (a), with its magnetization M indicated by the red arrows. An external field H induces a torque T in the body, as shown in (b). The body's Zeeman energy is minimized by aligning M with H as shown in (c). (Source: [26]).

Recent advances in smart materials and their applications have focused attention toward developing self-folding structures [10, 13, 14]. Several types of origami-inspired self-folding structures have been made in the past, including those utilizing the Miura-ori [12] and Waterbomb [14] patterns, origami cranes [10], barking dog [15] and an origami inspired forceps [16].

#### Compliant mechanisms

Some smart devices utilize materials that are relatively compliant, i.e. they have a relatively small Young's modulus, such as that of rubbers and elastomers [17–19]. A compliant material has both advantages and disadvantages in the context of self-folding structures. Folding structures typically possess stiff facets that experience little to no deformations, and thus any compliance would be undesirable in those regions/parts. Meanwhile, the creases of a foldable structure exhibit very large deformations, and can only be achieved by a relatively compliant material. Hence, folds are limited to finite curvatures, which has led to studying smooth folds in compliant structures [20].

Compliant mechanisms have been combined with active self-folding concepts for achieving a wide range of applications [10, 12, 21–23]. Some potential applications may seek a complex deformed shape upon actuation, i.e. target shape, that may not consist entirely of creases and flat surfaces, and instead possess regions of both flat and curved surfaces. Thus, materials like elastomers and polymers whose mechanical properties can be finely tuned are ideal candidates for foldable structures.

#### Magneto-active structures

Hard magnets have been used to actuate self-folding because the magnetic torque is strong enough to generate large displacements, especially in compliant mechanisms [13, 23–25]. Magnetic torque is possible due to the anisotropic magnetic properties of hard magnets, which have a preferred magnetic direction determined by their magnetization. The net magnetization  $\boldsymbol{M}$  of a material generates a net torque  $\boldsymbol{\tau}$  under an external magnetic field  $\boldsymbol{H}$  following:

$$\boldsymbol{\tau} = \boldsymbol{M} \times \boldsymbol{H}. \tag{1}$$

The magnetic torque is shown schematically in figure 1, where a magnetically susceptible body (red rectangle) is subjected to an external magnetic field (wide blue arrows) applied perpendicular to the direction of the body's net magnetization (red arrows). Consequently, an induced torque tends to rotate a body with volume V to minimize the Zeeman energy,  $E_{\rm Zeeman}$ , by aligning M with H.

$$E_{\text{Zeeman}} = -\mu_0 \int_V \mathbf{M} \cdot \mathbf{H} dV. \tag{2}$$

Magneto-active elastomers (MAEs) are a suitable class of magnetically actuated smart materials for self-folding structures due to their controllable magnetic properties and ease of fabrication into desired shapes. In recent work, MAEs have been fabricated using barium hexaferrite (BAM) particles embedded inside an elastomeric substrate while prescribing magnetic volume fraction and magnetic alignment direction during curing to control magnetic properties [27, 28].

# Electro-active structures

Electro-active polymers (EAPs) have also been deployed in active self-folding structures due to their ability to generate large displacements upon actuation [29–31]. Electrostrictive EAPs yield relatively high strains as they contract in the direction of the applied electric field and expand in the transverse directions. The actuation of EAPs in self-folding structures relies on at least one secondary layer of passive material attached to the EAP, which will constrain the deformation on one surface, inducing bending in the overall composite structure.

Multi-field actuated structures. In this work, we seek to combine magneto- and electro-active materials as possible layers and /or segments of a multifunctional structure. The combination of magneto- and electro-active materials in an active self-folding structure has been studied recently, and has several advantages [23, 31]. Two different actuation mechanisms enable more possible deformed configurations, e.g. multiple target shapes, as shown in figure 2. The example in figure 2 shows a bimorph actuator, which consists of an EAP and an MAE. The initial shape of the beam is straight, as shown in figure 2(a). With magnetic actuation the beam bends

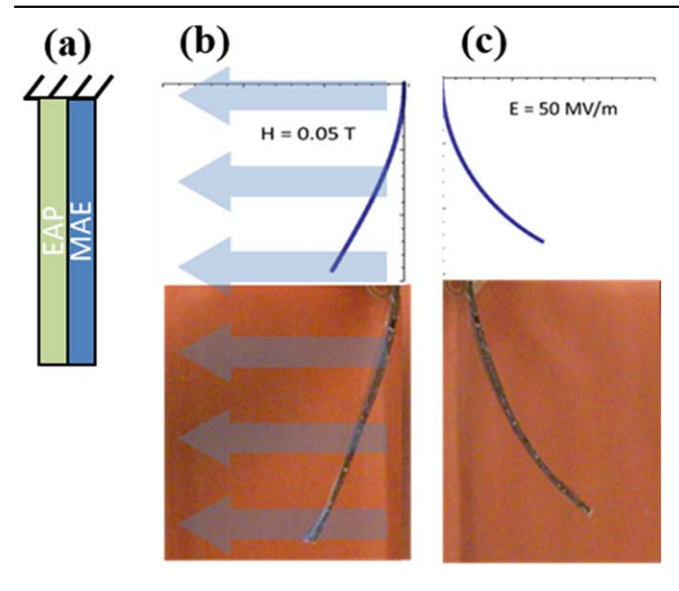


**Figure 2.** Bimorph composed of an EAP and MAE layer. Magnetic actuation yields bending towards the left, while electric actuation yields bending towards the right. (Source: [26]).

in one direction (figure 2(b)), while with electric actuation the beam bends in the opposite direction (figure 2(c)). When both fields are present simultaneously, however, the beam deforms into a more complex shape, highlighting the potential of multi-field actuation.

The purpose of this study is to understand how the choice of active material, configuration of that active material, device compliance, and layer geometries of a multi-field actuated device may influence its self-folding behavior. This goal is achieved by developing a model of the device's response, and then exploring the performance space associated with design variables within the model. The next section defines the geometry and configurations for our self-folding compliant beam structure. Next, the constraints of the design are determined based on manufacturing considerations, and the parameters are determined based on influence on self-folding actuation. Objective functions are next defined followed by implementation of a previously validated modeling approach to predict the multi-field actuation of the structure. Results of simulations across the design space are explored and analyzed in terms of the objective functions, allowing us to assess the efficacy of the objective functions and the relative significance of our chosen parameters.

Multi-field bimorph design. Multi-field bimorph actuators have been studied in active self-folding applications due to their ability to generate complex shapes [31, 32]. Consequently, they will be utilized as model segments in determining the structure for this study. In its most basic form, the multi-field bimorph consists of two layers, an MAE and EAP layer, as shown in figure 2. In this study, we will examine a more complex version of this basic bimorph by (1) dividing the MAE into separate, individual patches with alternating orientations, and (2) adding a passive layer. The segmentation of the MAE layer allows us to add a level of

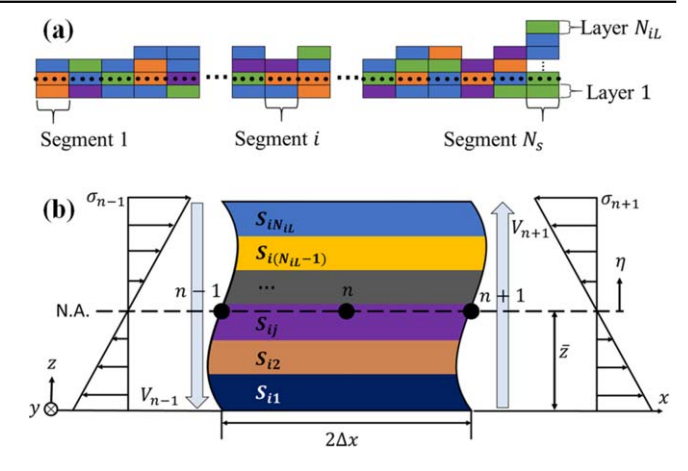


**Figure 3.** In (a), a schematic of a sample multi-field composite beam with an arbitrary number of segments, each consisting of an arbitrary number of layers, is shown. Each layer of each segment can have an arbitrary material type, denoted by the color code. In (b), a differential element of the composite beam at an arbitrary location along its length is provided, with cut faces subject to normal stresses and shear forces.

complexity to the deformed shape, and the ability to control the amount of magnetic material by varying patch sizes. The separation of the MAE layer into individual patches introduces the concept of a segmented beam. The passive layer is added to provide support to the segments lacking MAEs, while also constraining the EAP layer to promote bending in those segments.

# Methodology

To perform a formal design optimization of a multi-field, segmented self-folding structure, a modeling approach with appropriate functions must be chosen. The chosen model should be able to accommodate large displacements, electroand magneto-mechanical coupling, multi-layering, and segmentation. This section covers a model that can address each function and be used for an arbitrary optimization problem.

# Model framework

An existing modeling technique previously derived and validated by the authors is selected as a framework for predicting the deformed shape of the configurations allowing computation of the objective functions [33]. The model is based on a nonlinear, large displacement beam method for a composite beam of an arbitrary number of segments  $N_S$ , each composed of an arbitrary number of layers  $N_{iL}$ , as shown in figure 3(a). The indices i and j represent the segment and layer locations, respectively. Thus, any segment-layer coordinate along the length of the beam may contain a set of material and geometric properties,  $S_{ij}$ .

Let the beam of length L be discretized into p nodes. Consider a differential element between two points along the beam, n-1 and n+1, such that the element contains three

nodes. This type of three-node element is chosen for the convenience it provides when describing each element curvature by the curvature at node n, which falls at the center of the element. The governing equations can be written with two equilibrium equations for the differential element

$$\sum_{i=1}^{N} F_{x,ij} = 0, (3)$$

$$\sum_{i=1}^{N} M = 0,\tag{4}$$

where  $F_{x,ij}$  is the force in the direction of the beam's deformed neutral axis at segment i and layer j. The forces can be substituted with the integrals of the stresses over the surface of each cut, such that the sum of forces and moments, respectively, can be expressed as

$$\sum_{j=1}^{N_{iL}} \left[ \int_{A_{ij}} \sigma_{n+1,ij} dA_{ij} + F_{N,n+1} \right] - \sum_{j=1}^{N_{iL}} \left[ \int_{A_{ij}} \sigma_{n-1,ij} dA_{ij} \right] = 0, \quad (5)$$

$$\sum_{j=1}^{N_{iL}} \left[ \int_{A_j} \sigma_{n+1,ij} z dA_{ij} + 2V_{n+1} \Delta x \right] + \sum_{j=1}^{N_{iL}} \left[ -\int_{A_j} \sigma_{n-1,ij} z dA_{ij} \right]$$

$$+ \sum_{j=1}^{N_{iL}} \left[ 2\tau_{n,ij}(H) t_{\text{MAE}} w \Delta x \right] = 0,$$
(6)

where  $\sigma_{n,ij}$  are the stresses in the x direction at node n;  $A_{ij}$  is the cross-sectional area;  $\Delta x$  is the length between two nodes;  $\tau_{n,ij}(H)$  is a magnetic torque dependent on magnetic field strength; w is the width in the y direction;  $V_{n+1}$  is a shear force;  $F_{N,n+1}$  is the normal force; and z is the distance in the direction of the thickness, as defined in figure 3(b). The indices i and j refer to segment and layer locations, respectively. Each summation from j=1 (layer 1) to  $j=N_{iL}$  is shown separately to emphasize that the number of layers  $N_{iL}$  may be different for each node, n, n-1 and n+1.

The following constitutive equation is used for stress

$$\sigma_{n,ij} = Y_{ij}(\varepsilon_n + \varepsilon_{ij}^e(E)),$$
 (7)

in which  $\varepsilon_n$  is the elastic strain at node n, defined by beam kinematics

$$\varepsilon_j = -K(z + \overline{z}).$$
 (8)

The variable K is the curvature, and  $\overline{z}$  is the distance to the neutral axis. Meanwhile,  $\varepsilon_{ij}^e(E)$  is the electrostrictive strain as a function of an applied electric field E, determined from a microstructure-based electrostriction model for a nonlinear EAPs [34]. The model is based on averaging the strain-energy density of a semicrystalline microstructure, consisting of amorphous regions that behave like a hyperelastic material, and crystalline regions that behave like dipoles interacting with each other. The generalized form of the strain energy

density for a semicrystalline EAP is

$$\tilde{W} = \frac{(1 - v_c)}{A_{el}} \sum_{m}^{N_{\Phi}} \int_{sc}^{N_{\Phi}} f_{sc} (\Phi_n, \Theta_m) W_{8ch} (\Phi_n, \Theta_m, \lambda_m, C_l)$$

$$\times \sin \Phi \Delta \Theta \Delta \Phi + \frac{P_{sat}^2}{3v_c \epsilon (\lambda^{-1} \sin^2 \Phi_r + \lambda^2 \cos^2 \Phi_r)^{\frac{3}{2}}}$$

$$\times [\hat{\mathbf{p}}_1 \cdot \hat{\mathbf{p}}_2 - 3\hat{\mathbf{p}}_1 \cdot \hat{\mathbf{r}}\hat{\mathbf{p}}_2 \cdot \hat{\mathbf{r}}], \tag{9}$$

where  $\Phi_n$  and  $\Theta_m$  are microstructural parameters describing spatial orientations of crystalline regions,  $\lambda_m$  and  $C_1$  are elastic constants for the 8-chain hypelastic model  $W_{8\text{ch}}$  [35],  $f_{\text{sc}}$  is a probability density function,  $\hat{p}_1$  and  $\hat{p}_2$  are the unit vectors of two neighboring dipole moments separated by a vector whose unit vector is  $\hat{r}$ ,  $v_c$  is the volume fraction of the crystalline regions,  $\lambda$  is the macroscopic stretch,  $A_{\text{el}}$  is a constant of integration,  $P_{\text{sat}}$  is the saturation polarization, and  $\epsilon$  is the permittivity of the amorphous phase. The constitutive relation between the strain-energy density  $\tilde{W}$  and the Cauchy stress tensor T is given by

$$T = \frac{2}{I} \frac{\partial W}{\partial \mathbf{R}} \mathbf{B} + q\mathbf{I},\tag{10}$$

where q is a Lagrange multiplier to enforce an incompressibility constraint, I is the identity tensor, and  $B = F^T F$ , in which F is the deformation gradient tensor. The interactions between the dipoles changes as a function of the external field via the alignments of  $\hat{p}_1$  and  $\hat{p}_2$ , which shifts the equilibrium between the stresses generated from each phase. Finding the strain  $\varepsilon^e$  at which equilibrium is satisfied for each field strength is how the electromechanical coupling  $\varepsilon^e_{ij}(E)$  is determined.

The magnetic torque at each location,  $\tau_{n,ij}$ , is determined by the amount of magnetic material is present in the volume of magneto-active layer at each location i, j. The torque is a function of the relative angle of the point n, such that

$$\tau_{n,ij} = V_{\Delta} M_{n,ij} \times H, \tag{11}$$

where  $M_{n,ij}$  is the magnetization of the material at n,  $V_{\Delta} = \Delta x t_{ij} w$  is the volume of the magnetic layer in the differential element, and H is the externally applied magnetic field.

If a force  $F_{tip}$  is applied at one end of the beam, then the shear term V will be non-zero. Since the model is assuming large displacements, V cannot be assumed constant at each node. While this does not strictly satisfy equilibrium for each element, the difference between  $V_{n-1}$  and  $V_{n+1}$  can be assumed to reach 0 as  $\Delta x \to 0$ . Thus, if  $\Delta x \ll L$ , then the equilibrium can be approximated by (5) and (6).

The value of V at any node is a function of the deformation, as it will change based on the orientation of the element. For instance, if the beam is fixed on one end and  $F_{tip}$  is applied on the other end, which is free, then upon actuation, the beam will experience large deformations, and the shear force will change at each location depending on the orientation of the element. The orientations of the elements are dependent on the curvatures of the element and all those prior to it (starting from the fixed end, since it is more convenient to

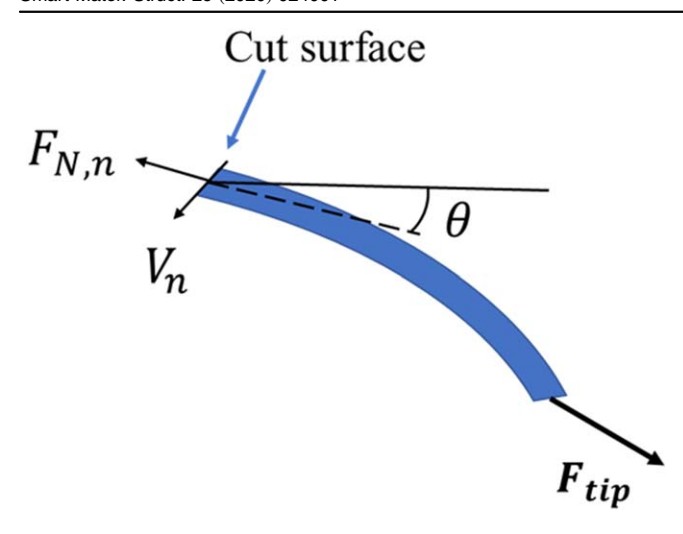


**Figure 4.** A tip force is applied to one end of the beam. The beam is cut at a location to show the angle of the location and the normal and shear forces acting at the cut surface.

apply the boundary condition this way). Similar arguments apply for the normal force,  $F_N$ . The normal and shear forces can be defined by

$$\mathbf{F}_{N,n} = F_{\text{tip},x} \sin \theta_n + F_{\text{tip},y} \cos \theta_n, \tag{12}$$

$$V_n = F_{\text{tip},x} \cos \theta_n + F_{\text{tip},y} \sin \theta_n, \tag{13}$$

where  $\theta_n$  is the angle of the element relative to the *x*-coordinate (counter-clockwise is positive). The angle and the shear and normal forces are illustrated in figure 4.

The governing equations are written for every possible three-node element across the beam, such that a system of equations can be written

$$C_{mn}K_n = f_n, (14)$$

where  $K_n$  are the unknown curvatures at each node,  $C_{mn} = C_{mn}(t_{ij}, \epsilon_{ij}, Y_{ij}, L, w)$  is a stiffness matrix,  $f_n = f_n(K, H, F_{tip})$  are the forcing terms. After solving for the curvatures, the curvatures can be transformed into coordinates in the deformed configuration,  $x_n$ , by a rotation matrix  $R_{mn}$  in the relation  $x_n = R_{mn}K_n$ . Details of the model can be found in [32].

Due to the nonlinearity of the problem, the model is solved by an iterative technique that utilizes the previous solution to determine the next solution at every step. At each iteration, the deformed shape solutions for given parameter sets S are calculated in MATLAB via the *vpasolve* numerical solver, and solutions of previous field increments are used as an initial guess for the next increment's solution. Between each iteration, the field strengths are incrementally increased to allow the solver to find the next solution. Thus, different sequences of electric or magnetic actuation can be simulated by changing the field strengths at each iteration in the order of our choosing. The order in which the fields are applied in multi-field actuation is significant because it is a pathdependent problem. A structure with the same configuration may yield different deformed shapes if the order of actuation is reversed. Multi-field actuation in experiments is typically conducted with the magnetic field applied first and held

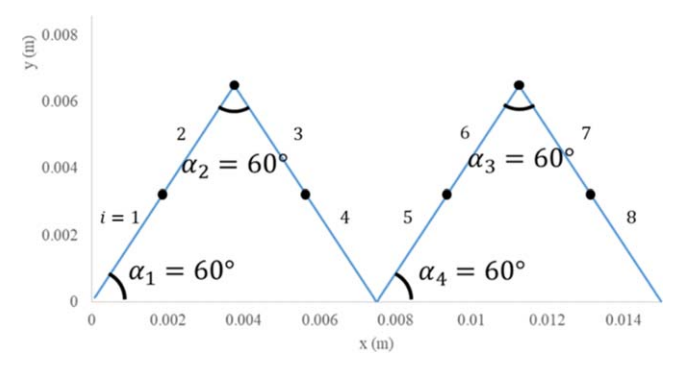


**Figure 5.** Target shape drawn as a line through the structure's neutral axis. Segments are identified between points along the shape's path. (Source: [26]).

constant, while the electric field is increased afterwards (to avoid prolonged electric actuation that may result in dielectric breakdown). As such, in the simulation the magnetic field is ramped first until it reaches its maximum, then while holding the magnetic field constant, the electric field is ramped until it also reaches its maximum value.

#### Objective functions

When considering the performance of a self-folding structure, a key metric is its ability to match the actuated shape it is designed to achieve. The target shape is defined in terms of a set of four panels and three folds, as shown in figure 5. To examine how closely the structure can reach ideal folded shape within the chosen design space, the fold angles are used. For example, all fold angles in the target shape, as defined in figure 5, are set to  $60^{\circ}$ .

The shape error objective function is computed in terms of the difference between the target shape's coordinates and the calculated coordinates under multi-field actuation at discrete points along the beam. Shape matching was originally proposed for rigid link mechanisms, and later applied to compliant mechanisms [36, 37]. Thus, it is an adequate measure of the self-folding structure's actuation capabilities.

$$f_{\text{shape}} = \sum_{i=1}^{N} \frac{(\boldsymbol{x}_{\text{model},i} - \boldsymbol{x}_{\text{target},i})^2}{L^2}.$$
 (15)

The target shapes coordinates are defined as  $x_{\text{target},i}$ , and the simulated coordinates are  $x_{\text{model},i}$  for i=1,2,...,N, where N is the number of discrete points along the beam's neutral axis (note the simulation methods yields the deformation along the beams' neutral axis). The differences between the locations of corresponding points on the simulated and target shape are divided by  $L^2$  (L is the total length of the beam) to normalize the error.

In terms of design, the cost of a self-folding structure is another important measure when evaluating the feasibility of the design. Two of our structural parameters, the length ratio and magnetization of the MAEs, directly influence how much magnetic material is present in the structure, and the magnetic material, BAM, is by far the most expensive material at approximately \$8000 per kg for nanoparticles (Sigma Aldrich). The magnetic cost of a design is defined as in



**Figure 6.** The location of the tip force is shown on the structure schematic.

equation (8) which depends on the total volume of BHF across all MAE patches,  $V_{\rm MAE}$ , a volume percentage, v, and the cost per volume, c.

$$f_{\text{cost}} = cvV_{\text{MAE}}.$$
 (16)

The total volume of the MAEs is dependent on the length parameter

$$V_{\text{MAE}} = 4w l_{\text{MAE}} t_{\text{MAE}}. \tag{17}$$

where  $l_{\rm MAE} = l_{\rm even}$  is the length of the MAE patch, and  $t_{\rm MAE}$  is the thickness of the MAE patch. The volume is multiplied by 4 so that it represents the total volume of all four MAE patches.

In addition, a third objective function is considered for the design optimization problem: the work performed by the structure on a force applied at the tip. This objective function is a significant addition to the optimization because (i) it is a metric of performance that can be directly applied to a gripper-like application [38, 39], and (ii) it has not been previously included in an optimization for a multi-field actuated device.

The force on the tip of the composite beam is assumed arbitrarily applied (see figure 6) such that the structure may pull the force to perform work.

The objective function for work is defined as

$$f_{\text{work}} = \int_0^s \mathbf{F_{tip}} \cdot d\mathbf{r}. \tag{18}$$

where  $F_{tip}$  is the applied tip force, dr is the incremental displacement of the tip, and s is the path traveled by the tip. If the composite is performing work on the tip force, then the dot product of  $F_{tip}$  and dr must be negative, since the composite should pull the force in the opposite direction of  $F_{tip}$ . Furthermore, the form of (18) is negative for actuation performance, and the more negative it is, the more work is done on the tip. This objective function is written in this form so that it can be minimized along with the other two objective functions.

#### Formal optimization setup

The results of the parameter study helped determine that each parameter influences the deformed shapes significantly. However, while the best designs contained a wide range of magnetizations and length ratios, the Young's modulus was consistently low. Consequently, the Young's modulus will be kept constant for the formal optimization. Additionally, a gap between the MAE patches was another common feature among the best designs, which means the optimization algorithm would benefit from a gap constraint.

The formal optimization problem is defined as:

Minimize: 
$$f_{\text{shape}}$$
,  $f_{\text{cost}}$ ,  $f_{\text{work}}$   
Subject to:  $C_{mn}K_n = f_n$   
 $x_n = R_{mn}K_n$   
 $0 \le M_k \le M_{\text{max}}$   
 $\sum_{i=1}^8 l_i = 1$   
 $l_i > 0$ , (19)

where the variables are

$$S = \{N_S, N_{iL}, M_{ij}, t_{ij}, \epsilon_{ij}, Y_{ij}, L, w, H, E\}.$$

Two constraints are added to ensure that segment length fractions,  $l_i$ , remain positive  $(l_i > 0)$  and sum to unity  $(\sum_{s=1}^{i=1} l_i = 1)$ .

For the optimization, a genetic algorithm developed by MATLAB, called *gamultiobj*, is chosen. This algorithm is a variant of the multiobjective genetic algorithm NSGA-II, and it well suited for problems with a relatively small number of variables. A basic flowchart of the genetic algorithm is provided in figure 7. Details on the base algorithm can be found in the original publication [40]. The genetic algorithm options are held at default except for the population size set to 100.

#### Case study

As a case study, consider a beam composed of a layer of EAP and a layer of passive material stretching along the entire length of the beam, with four MAE patches that are placed as shown in figure 8. Due to the MAE placements, and their magnetization orientations, the beam is divided into eight segments. The four-MAE-patch configuration allows the EAP layers in the two-layer segments to generate bending that can cooperate with the MAEs in folding the structure forming the so-called 'accordion' bending configuration (a double humped 'M' shape).

The direction of the force,  $F_{tip}$ , is assumed constant, and always in the x-direction. Thus,  $f_{work}$  can be simplified to

$$f_{\text{work}} = F_{\text{tip}} \partial_x,$$
 (20)

where  $\partial_x$  is the tip-displacement in the *x*-direction.

# Chosen parameters

In this subsection, the system parameters are explored such that the optimization problem can be narrowed by utilizing only a few key parameters, which will save computational costs.

Prior to any reductions to the parameters, consider the complete set of model parameters that describe the geometry, materials, and external stimuli, which are:

$$S = \{M_{ii}, t_{ii}, \epsilon_{ii}, Y_{ii}, L, w, H, E\}.$$
 (21)

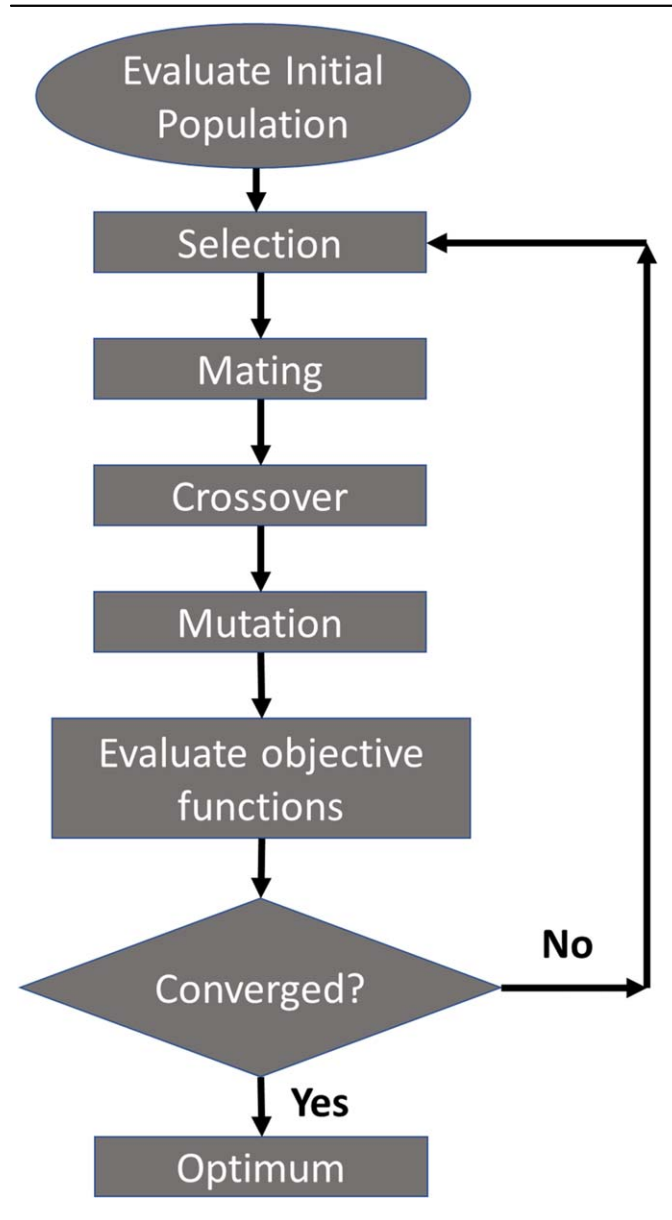


**Figure 7.** A basic flowchart of the genetic algorithm, starting from the initial population, and ending with the optimum population, which yields the Pareto front.

The parameters with subscripts are associated with layer j at ith segment:  $M_{ij}$  are the magnetizations;  $t_{ij}$  are the layer thicknesses;  $\epsilon_{ij}$  are the electrostrictive strains; and  $Y_{ij}$  are the Young's moduli. The parameters L and w are the length and width of the structure, respectively. The magnetic and electric fields are H and E, respectively.

In the generalized form, the structure must contain geometric and material information for every segment and layer, such that there are  $N_S$  segments with lengths  $l_i$ , yielding a total device length  $L = \sum_{i=1}^{N_s} l_i$  Total length L is kept constant, allowing focus on the relative lengths,  $l_i$ . All potential geometric and material parameters are listed in table 1.

Since EAPs are difficult to manufacture, and their properties are difficult to fine-tune, the EAP layers' properties will

be held constant for all segments present, resulting in  $\epsilon_{ij} = \epsilon$  when j = 1 and  $\epsilon_{ij} = 0$  otherwise.

We assume the width transverse to all layers and segments is constant, w, and all applied fields, E and H, are held constant globally (i.e. no spatial variation in either field).

The subset of parameters for the case study are reduced to:

$$S = \{M_2, M_4, M_6, M_6, l_1, l_2, l_3, l_4, l_5, l_6, l_7, l_8, Y_P\}.$$

where  $Y_P$  is the Young's modulus of the passive layer for all segments (i.e.  $Y_{i2} = Y_P$  for all i),  $M_i$  are the magnetizations of each MAE patch (i representing segment number), and  $l_i$  are the segment lengths. The layer indices, j, are dropped for the case study due to the predefined layer locations of each material (i.e. the passive layer is always at j = 1, EAPs at j = 2, and MAEs at j = 3).

These parameters are chosen due to their potentially large influences on the actuation of the structure, and consequently the objective functions.

For instance, one of the purposes of this study is to determine how compliance can affect the deformation and folding of a smart structure, making the Young's modulus of the materials an important variable. The Young's modulus of at least one of the materials is thus considered, and since varying the Young's modulus of an active material may result in nonlinear influences on its actuation properties, the passive layer's Young's modulus is selected as a parameter.

Another method of varying the bending stiffness along the length of the structure is by changing the lengths of the segments, which have different stiffnesses depending on the number of layers.

Beyond the stiffness of the structure, magnetization was considered as the third parameter, since the magnetization of an MAE is controllable during fabrication by adjusting the volume content of magnetic material of known magnetization response [41, 42]. Magnetization also influences both the actuation capability (see equation (1)), and the cost of the structure.

# Parameter study

A preliminary parametric study was performed prior to the optimization to understand the viability and usefulness of the chosen objective functions and a few key parameters [26]. The parameter study focused on two objective functions,  $f_{\rm shape}$  and  $f_{\rm cost}$ , and considered the effects of three parameters, the magnitude of the magnetization of the MAE patches, M, the Young's modulus of the passive layer,  $Y_p$ , and the ratio of the lengths of segments with the MAE patches to those without MAE patches,  $\Upsilon = l_{\rm odd}/l_{\rm even}$ . The reason for reducing the length parameters from all  $l_i$  to a ratio of the lengths of the odd segments to even segments is because all eight  $l_i$  was unwieldy for the parametric study and creating a length ratio for varying the lengths produces a single parameter that affects all segment lengths. The segment lengths were thus divided into two categories: odd and even numbered

**Table 1.** All possible geometric quantities and material properties for all layers in each segment for the chosen four MAE patch bimorph configuration.

	Geometric quantities				Material properties		
	Layer thickness						
	Segment length	$\overline{\text{Layer } j = 1}$	Layer $j = 2$	Layer $j = 3$	Layer $j = 1$	Layer $j = 2$	Layer $j = 3$
Segment $i = 1$	$l_1$	$t_{ m EAP}$	$t_P$	_	$\Gamma$ , $Y_{\rm EAP}$	$Y_P$	_
Segment $i = 2$	$l_2$	$t_{ m EAP}$	$t_P$	$t_{ m MAE}$	$\Gamma$ , $Y_{\rm EAP}$	$Y_P$	$M, Y_{\text{MAE}}$
Segment $i = 3$	$l_3$	$t_{ m EAP}$	$t_P$	_	$\Gamma$ , $Y_{\rm EAP}$	$Y_P$	_
Segment $i = 4$	$l_4$	$t_{ m EAP}$	$t_P$	$t_{ m MAE}$	$\Gamma$ , $Y_{\rm EAP}$	$Y_P$	$M, Y_{\text{MAE}}$
Segment $i = 5$	$l_5$	$t_{ m EAP}$	$t_P$	_	$\Gamma$ , $Y_{\rm EAP}$	$Y_P$	_
Segment $i = 6$	$l_6$	$t_{ m EAP}$	$t_P$	$t_{ m MAE}$	$\Gamma$ , $Y_{\rm EAP}$	$Y_P$	$M, Y_{\text{MAE}}$
Segment $i = 7$	$l_7$	$t_{ m EAP}$	$t_P$	_	$\Gamma$ , $Y_{\rm EAP}$	$Y_P$	_
Segment $i = 8$	$l_8$	$t_{ m EAP}$	$t_P$	$t_{ m MAE}$	$\Gamma$ , $Y_{\mathrm{EAP}}$	$Y_P$	$M, Y_{\mathrm{MAE}}$

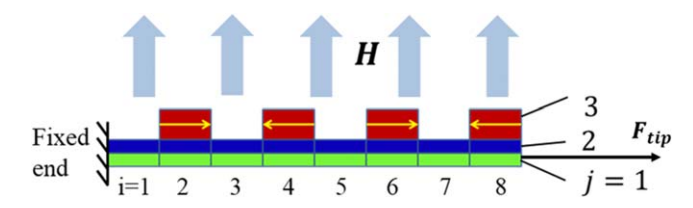


**Figure 8.** Schematic of a simple bimorph composed of eight segments with j layers, fixed on the left end. An external magnetic field H is applied upward. Layer 1 is an EAP (green); layer 2 is a passive material (blue); even numbered segments contain a layer 3, which is an MAE (magnetization directions signaled by yellow arrows). Dimensions are not to scale. (Source:[26]).

segments. A length ratio  $\Upsilon$  was defined as  $\Upsilon = l_{\rm odd}/l_{\rm even}$ , where  $l_i$  are the fraction of each segment length with respect to the total length of the structure.

The tip force was  ${\bf F}=0$ , since  $f_{\rm work}$  was not included in the study. The set of parameters for the parametric study can be shown as,

$$S^* = \{M, \Upsilon, Y_{i2} = Y_P\}, \tag{22}$$

where  $Y_P$  is the Young's modulus of the passive layer for all segments (i.e.  $Y_{i2} = Y_P$  for all i),  $\Upsilon$  is the length ratio of each segment with respect to each other. To generate symmetric torques,  $M_{ij}$  are held constant as well, hence  $M_{ij} = M$  for all even segments (i = 2, 4, 6, 8), at j = 3, and  $M_{ij} = 0$  for all others.

The same large displacement composite beam model discussed in the Methodology section was used to simulate the structures for the combinatorial set of parameters listed below, yielding 125 cases.

$$M = \{0.1, 0.2, 0.3, 0.45, 0.6\} T,$$
 (23)

$$Y_P = \{0.1, 0.5, 1, 5, 10\} Y_{EAP},$$
 (24)

$$\Upsilon = \{0, 1/3, 1, 3, 7\}. \tag{25}$$

The magnetization M was varied from 0.1 Tesla to 0.6 Tesla; the increments of the Young's Modulus of the passive layer,  $Y_P$ , were chosen relative to the Young's modulus of the EAP,  $Y_{\rm EAP}$ ; and the ratio of the lengths of two-layer to three-layer segments were varied from 0, which means the entire beam is covered with MAEs, to 7, which means the MAE patches were very short. A visual representation of the length ratios,  $\Upsilon$ , are shown in figure 9.

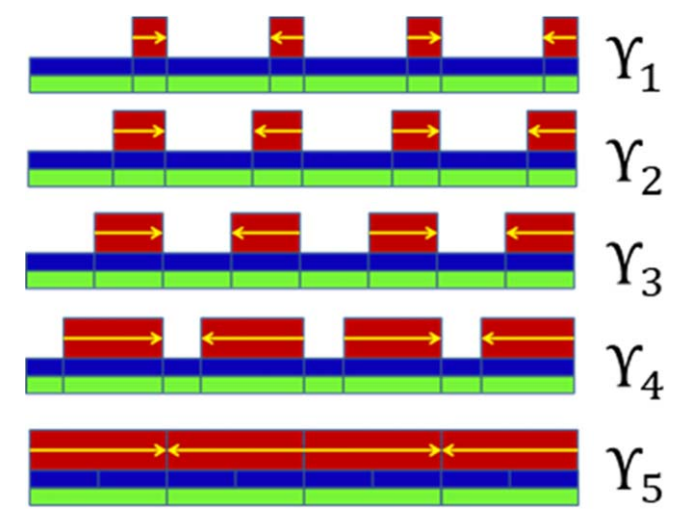


**Figure 9.** Chosen length parameter is visualized on a sample configuration. Red layers are MAEs, blue layers are passive, and green layers are EAPs. The yellow arrows on the MAE patches indicate direction of magnetization. From  $\gamma_1$  to  $\gamma_5$ , segments containing MAEs increase in length, while the remaining segments reduce in length. (Source: [26]).

**Table 2.** Material and layer properties for MAE, EAP, and the passive layer. (Source: [26]).

Parameter	MAE	EAP	Passive layer
t(μm)	520	30	$62$ $Y_P$ (varied)
Y(MPa)	3.5	200	

The remaining material properties and structure dimensions are borrowed from literature [26], and listed in table 2. The width was w=1 cm, and the length is L=3 cm. The maximum fields used were  $H_{\rm max}=30$  kA m<sup>-1</sup> and  $E_{\rm max}=50$  MV m<sup>-1</sup>. The fields were incremented at  $\Delta H=H_{\rm max}/15$ , followed by  $\Delta E=E_{\rm max}/15$ , totaling 30 steps to reach the final deformed shape.

Quantitative comparisons were made to determine how much the objective functions varied based on parametric changes. The simulations were assessed in a performance space to view the tradeoffs between the objectives, as shown

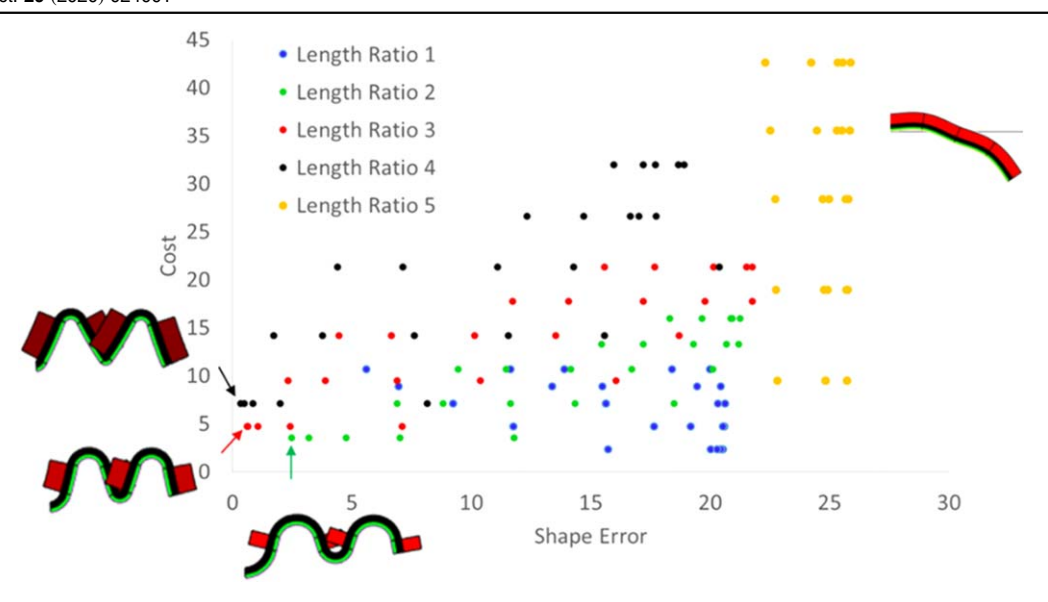


**Figure 10.** The performance space is shown. Each dot represents a simulation of a different combination of M,  $Y_P$ , and  $\gamma$ . The length ratio,  $\gamma$ , is indicated by color. The colored arrows on the bottom left indicate the best of the feasible designs. (Source: [26]).

in figure 8, where each point represents a feasible design. The points are also color coded to distinguish their length ratio. The best designs are expected to be in the lower left corner of figure 10.

Samples of the deformed shapes of the best designs, plotted with a custom graphics code in MATLAB that schematically represents the number of layers, segments, and material properties, are shown in figure 10. Each layer's color intensity signifies a specific property. The MAEs become more red as their magnetization M increases; the passive layer becomes more blue as  $Y_p$  increases; and the EAP is a static green to indicate constant electrostrictive properties. Recall that the MAEs are oriented in the directions shown in figure 8, with an external field upward. The layer thicknesses are not shown to scale, and thus any overlapping on the images does not imply physical contact between MAE patches from different segments. In reality, the thicknesses are small enough to allow very large curvatures.

Configurations within length ratio 1 were relatively low cost due to a low volume of MAEs, but they performed approximately in the middle of the total group of simulations. By contrast, length ratio 5 performed poorly across all parameter sweeps, and was the most costly due to the high volume of MAEs. Length ratios 2, 3, and 4 were more diagonally distributed on the  $f_{\rm shape}$  versus  $f_{\rm cost}$  map.

The three best performing configurations for each length ratio, as indicated by arrows in figure 10, were identified. Conversely, the worst designs are entirely of length ratio 5 (top right schematic in figure 10), showing little change as other parameters are varied. This may be a result of the high stiffness of the MAEs; when the MAEs are continuous across the length of the beam, no region of the structure exhibits relatively high bending, as in the case of the other length ratios. Thus, any attempt at achieving folding or even

moderate displacements may require spacing between the MAEs, which agrees with findings reported in the literature [31].

The effectiveness of the shape function's ability to gauge how well a design approximates the target shape was also studied by visually comparing the deformed shapes of designs along with their  $f_{\text{shape}}$  metrics. For example, the deformed shapes of the best designs in terms of shape are displayed in figure 11. The target shape is also displayed as an overlay on each simulated shape. It is evident from figure 11 that as the objective function  $f_{\rm shape}$  decreases among the best designs, the simulated shape better matches the target shape. In addition, the objective function also decreases as folding becomes more prominent at the creases between the MAE patches. This is further support for utilizing the objective function in seeking target shapes with sharp folds. However, this finding also implies that the length ratios 2, 3, and 4 are likely ideal starting locations for a formal optimization problem, and could potentially save significant time in searching for the best possible active self-folding design.

# Formal optimization problem results and discussions

The results of the parametric study informed choice of parameters such that the optimization problem would yield even better designs. Namely, the Young's modulus of the passive layer is removed as a parameter, and kept constant at  $Y_P = 0.1 Y_{\rm EAP}$ , since the lowest  $Y_P$  produced the best designs in the parametric study. Furthermore, the magnetizations and segment lengths are not assumed equal for each MAE patch or segment, respectively. As a result, the set of parameters for the optimization problem is

$$\mathbf{S} = \{M_2, M_4, M_6, M_6, l_1, l_2, l_3, l_4, l_5, l_6, l_7, l_8\}. \tag{26}$$

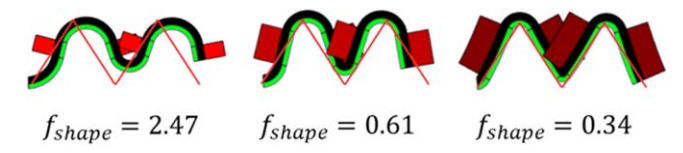


**Figure 11.** Deformed shapes of the three best designs with overlays of the target shape (red lines). From left to right: L2-M5-Y1, L3-M4-Y1, L4-M3-Y1. (Source: [26]).

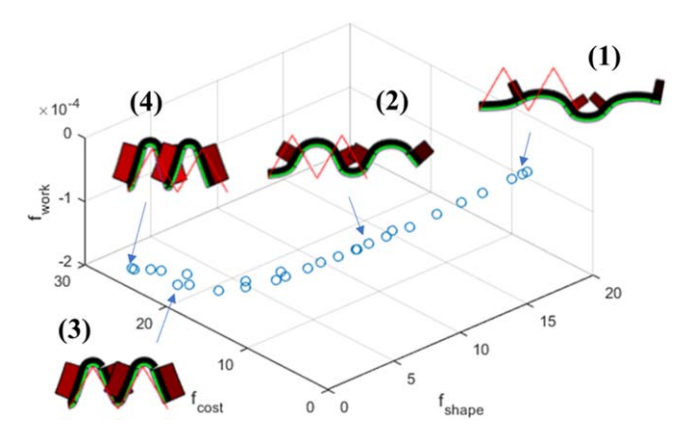


**Figure 12.** The Pareto front for the three objective functions is shown in a 3D plot, as obtained from the genetic algorithm. Each point represents an optimal individual based on the objective functions.

The same constants from the parameter study are used for the optimization (see table 2). Additionally, a tip force is present in the optimization problem to calculate  $f_{\rm work}$ . The magnitude of the force is manually chosen to be 10 mN, and the magnetic field is increased to  $70 \, {\rm kA} \, {\rm m}^{-1}$ , which allows the structure to fold beyond the target shape at the configuration with the highest BHF content.

Since a genetic algorithm is employed for optimization, an initial search population must be selected. MATLAB's genetic algorithm, gamultiobj, can generate a default initial population, but a few preliminary optimization iterations utilizing the default initial population did not yield a diverse set of optimal designs. To address this issue, the initial population is modified by (1) adding the best designs from the parametric study, which can aid the algorithm in finding more optimal spaces, and (2) designs with more extreme segment lengths, particularly those with  $\Upsilon > 7$ , are introduced, which helps promote diversity in the initial population. The custom designs selected for the initial population do not add to the total population size, which is 100. Consequently, the remaining individuals in the initial population are generated by the default algorithm.

The optimization is performed with the genetic algorithm and allowed to converge toward a Pareto front for minimizing the three objective functions, shown in figure 12. The axes represent the three objective functions, and each circle in the Pareto front represents an optimal individual whose performances in terms of the objective functions cannot be improved by changing their parameters. The path of the Pareto front is 3-dimensional and contains individuals with a range of performances in terms of the objective functions. For example, there are individuals with high shape error, low cost

**Table 3.** Objective function evaluations and magnetizations for the highlighted in designs in figure 12.

	D1	D2	D3	D4
$f_{shape}$	16	5.1	0.12	0.71
$f_{cost}$ (\$)	1.6	7.1	17.3	25.4
$-f_{work}$ (10 <sup>-4</sup> )	0.12	0.84	1.49	1.81
$M_2$ (T)	0.093	0.19	0.36	0.45
$M_4(T)$	0.037	0.20	0.29	0.57
$M_6$ (T)	0.15	0.31	0.24	0.45
$M_8$ (T)	0.068	0.19	0.31	0.32

and low work on one end, and those with low shape error, high cost, and high work on the other end. Individuals at around the mid-point of the Pareto front have a more balanced performance in terms of the three objectives.

Samples of the deformed shapes of feasible designs on the Pareto front are provided in figure 12. Design 1 has the highest shape error (16), lowest cost (\$1.6), and least work done (0.12). Design 2 has moderate shape error (5.1), cost (\$7.1), and work (0.84). Design 3 has the least shape error (0.12), and high cost (\$25.4), and work (1.49). Design 4 has the low shape error (0.71), highest cost (\$25.4), and the best work (1.81). A summary of these results are listed in table 3.

The design with the highest shape error (or least matching shape), Design 1, has very short MaE patches, while those with the best matching shapes near the other end of the Pareto front, such as Designs 3 and 4, have the largest MAE patches. In between designs 1 and 4, there is a gradual change in MAE patch size. Interestingly, the lengths of the segments containing MAEs (i.e. even numbered segments) are relatively even within each Pareto individual. Since there was no constraint on the relative lengths (as there were in the parametric study), these results imply that symmetry may promote shape matching.

Similar to the MAE patch lengths, the magnetizations of MAE patches also gradually change along the Pareto front. Design 1's MAE patches have the least magnetization among all designs, while Design 4's patches have the highest magnetizations. The values of the magnetizations for each patch on all four selected designs are listed in table 3.

Another notable trend is that the magnetization of the patch on the fourth segment,  $M_4$ , is lowest among the patches in Design 1, but highest in Design 4. In fact,  $M_4$  in Design 4 is greater than  $M_4$  in Design 1 by more than a factor of 15, the largest factor across any two magnetizations. Thus, this means that the system is highly sensitive to  $M_4$  (combined with a steady change in MAE patch lengths), perhaps more than any other parameter that was used in the optimization. Similarly, the system is also sensitive to  $M_2$ , which changes by almost a factor of 5 between Design 1 and Design 4.

Another trend in the Pareto space is that  $M_8$  remains the lowest in almost every design. It is likely that  $M_8$  is lowest in most designs since it is located on the 8th segment, which is the free end of the beam. Regions near the free end of the beam may not require as much torque, which can be useful

information when designing a magnetically-actuated cantilever device.

The only exception to this rule is found in Design 3. Unlike the other selected designs, Design 3 has an  $M_8$  that is not the weakest of its MAE patches. In fact, the magnetizations of the MAE patches in Design 3 are relatively uniform. The smallest magnetization  $(M_6 = 0.24 T)$  in Design 3 is only 66% of the largest magnetization ( $M_2 = 0.36 T$ ). Compared to the designs (25% for Design 1, 61% for Design 2, and 57% for Design 3), this is the closest relative magnetizations between the weakest and strongest MAE patches in a design. There is also better symmetry in Design 3 than in any other design. The outer MAE patches ( $M_2$  and  $M_8$ ) have the highest magnetizations while the inner MAE patches ( $M_4$ and  $M_6$ ) have the lowest. Conversely, Designs 1 and 2 are asymmetric with  $M_6$  being greater than the next strongest MAE patch in each design, and without a balance on the other end of the beam (i.e.  $M_2$  or  $M_4$ ). Similarly, Design 4 is skewed toward the fixed end of the beam. Thus, the results imply that symmetry and relatively uniform magnetizations are best for matching the chosen target shape. This is not a coincidence, since the chosen target shape is also symmetric about the midpoint. However, it is also important to point out that the magnetizations and lengths of Design 3 are not exactly uniform or symmetric, which would be expected for the chosen target shape. This is likely due to (i) a bias with the initial population, which led to a convergence toward a non-symmetric or uniform design in terms of magnetizations, and (ii) a relatively low population size of 100. It may also be due to the boundary conditions (fixed end, and free end with applied load) combined with numerical approximation errors.

Nonetheless, despite the optimization results not being exactly symmetric as expected for some of the designs, the methodologies presented in this work have yielded quick results that perform significantly better than any design found via the parameter study. For instance, the lowest shape error acquired from the parameter study was 0.34, which is nearly three times greater than the lowest shape error from the optimization (0.12, Design 3). Similarly, the lowest cost from the parameter study, \$3.5 (L3-M4-Y1), is more than twice as much as the lowest cost of a Pareto design from the optimization, \$1.6 (Design 1). Thus, the optimization method improved upon the parameter study in terms of the objective functions, and it took about 40 h to run on a 100-core cluster, which is a feasible computational speed for results several times better than any results that could be obtained from trial and error, or a parametric study.

Based on this analysis, if an application requires ideal shape matching, then the best design should have relatively high, uniform, and symmetric magnetizations and long MAE patches throughout the length of the device as in Design 3. If an application prioritizes costs, then shortening the lengths of the MAE patches and reducing their magnetizations, while maintaining patch placement symmetry, as in Design 1, is ideal. For maximizing work, the magnetizations should be increased near the limits, with  $M_4$  the highest among the MAE patches, as in Design 4. If an application requires more

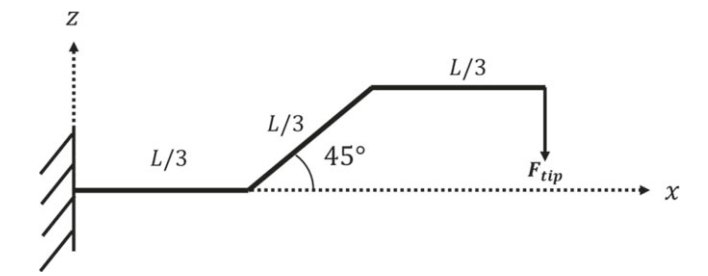


**Figure 13.** The second target shape resembles a ramping function. The shape has three regions of equal length, L/3. The tip force is applied in the vertical direction as shown.

complex priorities, then one can select another design based on the trade-offs in the Pareto front that meet their needs.

#### Formal optimization problem for a second target shape

To test the robustness of the optimization methods presented in this work, a second target shape is considered. The shape is presented in figure 13, and resembles a ramping function. This shape is chosen because it is not achievable with a simple unimorph and it also includes ideal folds. Furthermore, unlike the M-shape (figure 5) used for the target shape in the first optimization problem, the ramping target shape only contains three straight regions. The ramping region of the new target shape is at a 45° angle to the horizon, and the tip force is applied in the vertical direction, as shown in figure 13.

Due to the change in the direction of the tip force,  $F_{\rm tip}$ , the objective function associated with work,  $f_{\rm work}$  can be written as

$$f_{\text{work}} = -F_{\text{tip}}\partial_z. \tag{27}$$

Since the sign of  $f_{\rm work}$  is negative again, it can be appropriately substituted for into the optimization problem, which aims to minimize all objective functions.

While a parameter study was used to provide the initial population of the first optimization problem (M-shaped target) with high-performing designs, the initial population of the second optimization problem (ramping-shaped target) is not supplied with such designs. Instead, a default, randomly generated population is used for generation 0. A lack of quality designs in the initial population will likely limit the performance of the optimization for the second target shape, but it will help understand how well the optimization can perform for a second shape, even without a parameter study.

The parameters are the same as in the first target shape optimization, shown in (26). The results of the genetic algorithm are shown in figure 14. The three selected designs in figure 14 with annotated deformed shapes represent the designs with the best shape, work, and cost, i.e. the designs with the best values of the individual objective functions. Design 1 is best in cost (\$1.3) but worst in shape (97) and work (0.11  $\mu$ Nm); design 2 is best in work ( $-1.0 \mu$ Nm) but suffers in shape (32) and cost (\$19); and design 3 is best in shape (0.38) but not ideal in work ( $-0.18 \mu$ Nm) or cost (\$25). While designs 1 and 2 appear to perform well in their areas of strength (cost and work, respectively), design 3

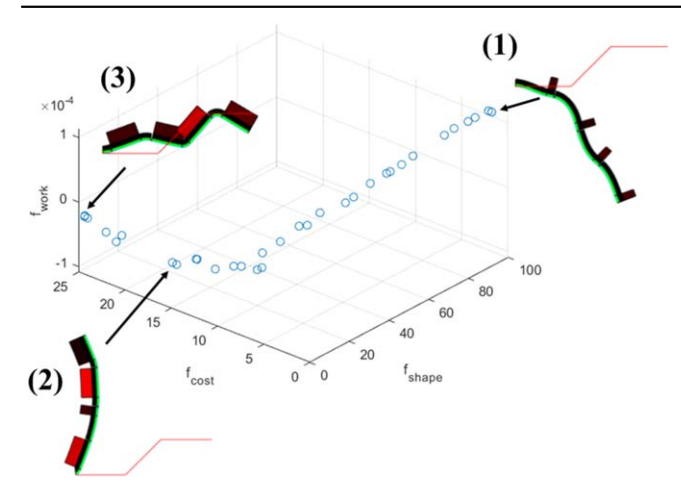


**Figure 14.** The Pareto front for the three objective functions for the ramping target shape is shown in a 3D plot, as obtained from the genetic algorithm. Each point represents an optimal individual based on the objective functions.

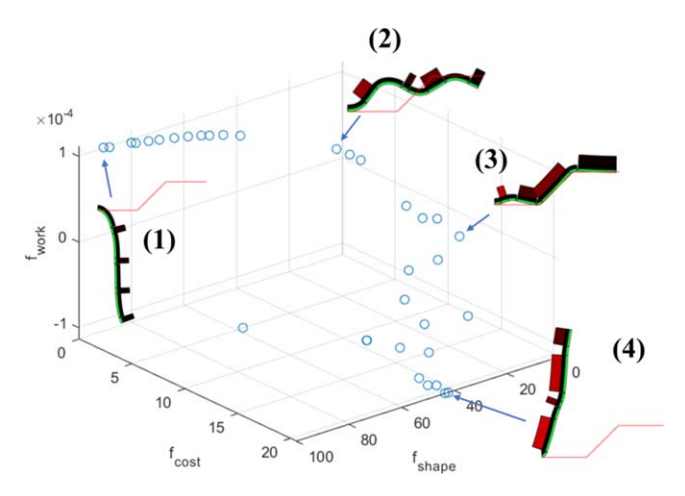


**Figure 15.** The Pareto front is shown in a 3D plot, as obtained from the genetic algorithm with the ramping-shape objective function. For this Pareto front, the initial population included a manually selected design that performed well in matching the ramping shape. Each point represents an optimal individual based on the objective functions.

performs poorly both quantitively and qualitatively. For instance, its shape error, which is 0.38, is much higher than the best design for the M-shape, which had a shape error of 0.12. Furthermore, the deformed shape of design 3 does not resemble the chosen ramping target shape. This is likely due to a lack of 'good' designs in the initial population, which are harder to obtain with a relatively small population size of 100.

To test the effects of the initial population, another genetic algorithm is carried out with one design that is manually selected and added to the initial population. The design is chosen based on its relatively well matching deformed shape to the ramping target shape, with an error of 0.2. The results of the second genetic algorithm for the ramping target shape are presented in figure 15, which shows a Pareto front including selected designs performing best in the three objective functions.

**Table 4.** Objective function evaluations and magnetizations for the highlighted designs in figure 12.

	D1	D2	D3	D4
$f_{shape}$	95	1.3	0.04	43
$f_{cost}$ (\$)	1.2	6.4	11	20
$-f_{work}$ (10 <sup>-4</sup> )	-11	1.8	2.8	10
$M_2$ (T)	0.09	0.34	0.46	0.49
$M_4(T)$	0.07	0.12	0.18	0.28
$M_6$ (T)	0.04	0.24	0.28	0.44
$M_8$ (T)	0.01	0.05	0.02	0.20

Figure 15 contains four selected designs with their deformed shapes annotated. Design 1 performs best in cost; design 3 performs best in shape; and design 4 performs best in work. Designs 1 and 4 are very close to their counterparts from figure 14, which was obtained without a custom initial population. Meanwhile, Design 3 shows significant improvement over the best shape achieved in figure 14. In fact, the best design in terms of shape from figure 15 has a shape error of 0.04, which is an order of magnitude better than the best shape design from figure 14, which was 0.38. The parameters and performances of the four designs are presented in table 4.

Since we are seeking to find more negative work values, Design 1's positive work means there is no work being performed in the preferred direction. Thus, Design 1 would not be a practical choice for an application requiring at least some level of shape matching and work (it does not perform any work on the tip force). As an alternative to Design 1, Design 2 is also annotated in figure 15, which is the cheapest design that performs work on the tip force and comes close to matching the ramping target shape.

#### **Conclusions**

The purpose of this study was to set up a multi-objective design optimization problem for a multi-field actuated device employing magneto- and electro-active materials. An existing model accommodating large displacements and magneto- and electromechanical coupling was used, and extended for the application of a tip-force on one end of the beam. The design optimization problem was written for a multi-field actuated device consisting of several parameters, including number of segments and layers; thicknesses, lengths, and all material properties. Three objective functions were chosen: (1) shape error, i.e. the error between calculated and target shapes, (2) cost, and (3) work performed on the tip load.

To assist the formal optimization, a case study consisting of eight segments was considered, reducing the number of parameters and possible combinations of materials at each layer and segment. Furthermore, a preliminary parameter study was performed on the eight-segmented bimorph structure design to predict how a set of parameters affect the self-folding of the structure. Only the shape and cost objective functions were considered. The parameters chosen for the study were the

magnetization of the MAEs, the Young's modulus of the passive layer, and the length ratio of the segments. The results of the parameter study found that each parameter influenced shape approximation by almost an order of magnitude. Furthermore, the parameter combination that yielded the lowest shape error performed significantly better in both matching the target shape and achieving self-folding, which implies that the chosen shape objective function was adequate in assessing the degree of folding.

The results of this parameter study were used in determining the constraints and initial search population for the optimization algorithm. For example, relatively long MAE patches were used as a good starting point, since long MAE patches performed best among all length ratios in terms of folding. Configurations with MAE patches covering the entire length of the structure were omitted from the design space, since they could not produce fold-like patterns, while very small MAE patches were also eliminated since they did not generate enough torque. The parameter study also highlighted the significance of the Young's modulus of the passive layer, and suggested that self-folding requires very low Young's modulus of the passive layer with respect to the EAP layer. Thus, the Young's modulus was preset to the lowest value from the parametric study.

The multi-objective optimization yielded a Pareto front with a range of optimal individuals to select from based on the priority of the design. The Pareto front showed optimal designs in terms of cost, shape, and work. Nearly all designs were relatively symmetric in length segments, and contained a range of magnetizations. However, it was found that some MAE locations, such as  $M_4$ , may play a more significant role in actuation than others, especially in terms of shape approximation. Furthermore, the results yielded much better designs in terms of the chosen objective functions than any design obtained from the parameter study. It can be concluded from the results that the optimization method is an improvement over trial and error or parametric studies, and performs well in terms of computational speed.

The optimization problem is also tested for robustness by trying another target shape, which resembles a ramping shape. The genetic algorithm is run twice, once with a default (random) initial population, and one with a custom initial population containing a design performing well in matching the shape. The results of the second optimization problem show that adding a well-performing individual to the initial population can significantly improve the best shape-matching design on the Pareto front, by up to an order of magnitude in shape error. Furthermore, given a well-chosen initial population, the optimization method proves to work well in optimizing for the chosen objective functions, outperforming even the well-chosen designs.

Future improvements on the optimization can be made through adjustments to the settings. For example, different custom initial populations can yield different Pareto fronts, which can potentially contain more optimal individuals. Particularly, the diversity of the initial population plays a significant role, which can be studied further. In addition, the

number of elites was not modified, which could also influence which traits are passed down in the genetic algorithm.

Additionally, several variables were not considered in this study, such as the width and length of the structure, Young's moduli of the MAE and EAP, and the electrostrictive properties of the EAP. Both the electric and magnetic fields were kept constant for the simulations, and we chose a specific order of actuation (magnetic field first, and then electric field). Varying any of these parameters may alter influence the self-folding behavior of the structure, which means that the scope of this study is limited to structures with similar configurations and constants. As a result, a more thorough investigation utilizing a larger parameter space may generate more optimal Pareto fronts. However, our results show this methodology may be useful for the multi-objective optimization of arbitrary multi-field-active, compliant, self-folding structures.

# **Acknowledgments**

We gratefully acknowledge the support of the National Science Foundation EFRI grant number 1240459, the National Science Foundation grant number MEP 1762188, and the Air Force Office of Scientific Research. Sections of this article have been previously published by ASME in [26].

#### **ORCID iDs**

Anil Erol https://orcid.org/0000-0003-4265-8153

# References

- [1] Schenk M and Guest S D 2011 Origami folding: a structural engineering approach *Origami 5: Fifth International Meeting of Origami Science, Mathematics, and Education* (Boca Raton, FL: CRC Press)
- [2] Peraza-Hernandez E A et al 2014 Origami-inspired active structures: a synthesis and review Smart Mater. Struct. 23 094001
- [3] Onal C D *et al* 2015 Origami-inspired printed robots *IEEE/ASME Trans. Mechatronics* **20** 2214–21
- [4] Lee D-Y *et al* 2013 Deformable wheel robot based on origami structure 2013 IEEE Int. Conf. on Robotics and Automation (ICRA) (Piscataway, NJ: IEEE)
- [5] She Y, Carter J H and Hai-Jun S 2015 A transformable wheel robot with a passive leg 2015 IEEE/RSJ Int. Conf. on. Intelligent Robots and Systems (IROS) (Piscataway, NJ: IEEE)
- [6] Onal C D, Robert J W and Rus D 2013 An origami-inspired approach to worm robots *IEEE/ASME Trans. Mechatronics* 18 430–8
- [7] Filipov E T, Tachi T and Paulino G H 2015 Origami tubes assembled into stiff, yet reconfigurable structures and metamaterials *Proc. Natl Acad. Sci.* 112 12321–6
- [8] Martinez R V et al 2012 Elastomeric origami: programmable paper-elastomer composites as pneumatic actuators Adv. Funct. Mater. 22 1376–84

- [9] Martinez R V et al 2013 Robotic tenta cles with threedimensional mobility based on flexible elastomers Adv. Mater. 25 205–12
- [10] Felton S et al 2014 A method for building self-folding machines Science 345 644–6
- [11] Li S, Vogt D, Rus D and Wood R 2017 Fluid-driven origamiinspired artificial muscles *Proceedings of the National* Academy of Sciences of the United States of America
- [12] Felton S M et al 2013 Self-folding with shape memory composites Soft Matter 9 7688–94
- [13] Cowan B M and von Lockette P 2017 Trade space exploration of a magnetically actuated miura-ori structure. Conference on Smart Materials, Adaptive Structures and Intelligent Systems
- [14] Bowen L et al 2015 Development and validation of a dynamic model of magneto-active elastomer actuation of the origami waterbomb base J. Mech. Robot. 7 011010
- [15] Bowen L et al 2017 Design, fabrication, and modeling of an electric-magnetic self-folding sheet J. Mech. Robot. 9 021012
- [16] Edmondson B J et al 2013 Oriceps: origami-inspired forceps ASME 2013 Conf. on Smart Materials, Adaptive Structures and Intelligent Systems (American Society of Mechanical Engineers)
- [17] Howell L L 2001 Compliant Mechanisms (New York: Wiley)
- [18] Kota S and Ananthasuresh G K 1995 Designing compliant mechanisms Mech. Eng.-CIME 117 93–7
- [19] Bruns T E and Daniel A T 2001 Topology optimization of nonlinear elastic structures and compliant mechanisms Comput. Meth. Appl. Mech. Eng. 190 3443–59
- [20] Peraza-Hernandez E and Alexander E 2016 Kinematics, structural mechanics, and design of origami structures with smooth folds *PhD Thesis* Texas A&M University
- [21] Calogero J et al 2017 Optimization of spatially distributed contact-aided compliant mechanisms in a dynamic structure ASME 2017 Conf. on Smart Materials, Adaptive Structures and Intelligent Systems (American Society of Mechanical Engineers)
- [22] Saggere L and Kota S 1999 Static shape control of smart structures using compliant mechanisms AIAA J. 37 572–8
- [23] Frecker M I 2003 Recent advances in optimization of smart structures and actuators J. Intell. Mater. Syst. Struct. 14 207–16
- [24] Crivaro A et al 2016 Bistable compliant mechanism using magneto active elastomer actuation J. Intell. Mater. Syst. Struct. 27 2049–61
- [25] Sung E et al 2016 Characterization of self-folding origami structures using magneto-active elastomers ASME 2016 Int. Design Engineering Technical Conf. and Computers and Information in Engineering Conf. (American Society of Mechanical Engineers)
- [26] Erol A, von Lockette P and Frecker M 2018 Parameter study of a multi-field actuated, multilayered, segmented flexible composite beam ASME 2018 Conf. on Smart Materials, Adaptive Structures and Intelligent Systems (American Society of Mechanical Engineers)
- [27] von Lockette P R, Kadlowec J and Koo J-H 2006 Particle mixtures in magnetorheological elastomers (MREs) *Proc.* SPIE 6170 61700T

- [28] von Lockette P and Sheridan R 2013 Folding actuation and locomotion of novel magneto-active elastomer (MAE) composites ASME 2013 Conf. on Smart Materials, Adaptive Structures and Intelligent Systems (American Society of Mechanical Engineers)
- [29] Ahmed S, Ounaies Z and Arrojado E A F 2017 Electric fieldinduced bending and folding of polymer sheets Sensors Actuators A 260 68–80
- [30] Ahmed S, Arrojado E and Ounaies Z 2016 Realization of origami-inspired smart structures using electroactive polymer (EAP) ASME 2016 Conf. on Smart Materials, Adaptive Structures and Intelligent Systems (American Society of Mechanical Engineers)
- [31] Zhang W et al 2017 Finite element analysis of electroactive and magnetoactive coupled behaviors in multi-field origami structures ASME 2017 Conf. on Smart Materials, Adaptive Structures and Intelligent Systems (American Society of Mechanical Engineers)
- [32] Erol A *et al* 2016 On the modeling and experimental validation of multi-field polymer-based bimorphs *ASME 2016 Conf. on Smart Materials, Adaptive Structures and Intelligent Systems* (American Society of Mechanical Engineers)
- [33] Ahmed S et al 2015 Electric field responsive origami structures using electrostriction-based active materials Proc. SPIE 9432 943206
- [34] Erol A, Ahmed S, Ounaies Z and von Lockette P 2019 A microstructure-based approach to modeling electrostriction that accounts for variability in spatial locations of domains *J. Mech. Phys. Solids* **124** 35–62
- [35] Arruda E M and Mary C B 1993 A three-dimensional constitutive model for the large stretch behavior of rubber elastic materials J. Mech. Phys. Solids 41 389–412
- [36] Murray A P, James P S and Brian M K 2008 Kinematic synthesis of planar, shape-changing rigid-body mechanisms J. Mech. Des. 130 032302
- [37] Jovanova J et al 2016 Target shape optimization of functionally graded shape memory alloy compliant mechanism ASME 2016 Conf. on Smart Materials, Adaptive Structures and Intelligent Systems (American Society of Mechanical Engineers)
- [38] Shian S, Bertoldi K and Clarke D R 2015 Dielectric elastomer based 'grippers' for soft robotics Adv. Mater. 27 6814–9
- [39] Zhang W et al 2018 Parametric design of a soft gripper actuated using the electrostrictive PVDF-based terpolymer ASME 2018 Conf. on Smart Materials, Adaptive Structures and Intelligent Systems (American Society of Mechanical Engineers)
- [40] Deb K et al 2002 A fast and elitist multiobjective genetic algorithm: NSGA-II *IEEE Trans. Evol. Comput.* **6** 182–97
- [41] Haussener T K 2016 Determining the effects of increased volume fraction of barium hexaferrite as a magnetic filler in magneto-active elastomers *MSc Thesis* The Pennsylvania State University
- [42] Breznak C and von Lockette P 2016 Evolution of the magnetization response of magneto-active elastomers made with hard-magnetic M-type barium hexaferrite particles MRS Adv. 1 39–43